Bridge expansion after coalescence of two droplets in air: inertial regime

Véronique Chireux,[1] Philippe Tordjeman,[1] and Frédéric Risso[1, a)]
Institut de Mécanique des Fluides de Toulouse, IMFT, Université de Toulouse, CNRS - Allé Camille Soula, 31400 Toulouse, France

(Dated: 21 May 2021)

When two liquid droplets approach at negligible velocity in air, their coalescence spontaneously occurs by jump-to-contact instability and a connecting bridge joining the two facing interfaces at the nanoscale is created. We report experimental investigations of the expansion of this initial bridge by means of high-speed imaging. By considering droplets of water, polydimethylsiloxane or paraffin of a few hundred micrometers, we investigate regimes where inertia takes a major role. Depending on the Ohnesorge number Oh, the dynamics of the bridge differs a lot. For Oh≈1, the initial flow is rapidly attenuated and the connecting bridge between the two droplets adopts a smooth parabolic shape. The maximum interface curvature and the minimum liquid pressure remain at the bridge centre. The expansion is thus caused by the capillary pressure that drives the fluid towards the center. At small Oh, in the inertial regime, the length of the initial bridge grows at constant speed and the bridge expansion can be described by the propagation of non-dispersive capillary wave packets. The central part of the bridge takes a cylindrical shape connected to the droplets by a narrow region of very large curvature. At the resolved scale, the interface exhibits slope discontinuities. By considering dihedral potential flows that result of the presence of the slope discontinuities, we show that the apparent angle made by the interface controls the flow-rate that enters the bridge and thus determines its radial expansion.

[a)]Electronic mail: frisso@imft.fr

Bridge expansion after coalescence of two droplets in air

I. INTRODUCTION

Coalescence is a fundamental mechanism that drives the size growth of droplets in numerous natural or man-made processes, from clouds formation[1] to emulsions separation[2]. It is a complex phenomenon that involves several mechanisms[3–6] at various scales[7]. The dynamics of the droplets coalescence is extensively discussed in literature from experiments, theoretical investigations and numerical simulations. There is a large consensus that the Ohnesorge number, $\mathrm{Oh_m} = \mu/\sqrt{\rho\gamma R_m}$, where μ and ρ are the dynamic viscosity and density of the droplet liquid and γ is the surface tension, is the physical parameter which controls the dynamics of the microscopic liquid bridge expansion between two droplets.

Here, R_m is minimum of the radius of the bridge connecting two droplets and characterizes the scale flow when the droplets merge. Assuming that the droplets touch at one point, the initial dynamics occurs at $\mathrm{Oh_m} \gg 1$ and is dominated by viscous effects. In this Stokes regime, the growth of the connecting bridge follows a scaling law in time, $R_m \sim t\ln t$, but the dynamics is inextricably linked to the droplet contact singularity[8]. Even if the question is always open for droplet coalescence in liquid, the pure Stokes regime was never observed experimentally for droplet coalescence in air[9,10]. Indeed, recent experiments by Atomic Force Microscopy show that the droplet coalescence in air is due to the effects of attractive van der Waals forces[11,12]. These forces induce a jump-to-contact instability[13,14] which occurs when the two droplets are at a distance of ten nanometers (15 nm for droplets larger than 1 μm). The jump-to-contact characteristic time is between 10^{-9} and 10^{-7} s, depending on the liquid viscosity and the surface tension.This hydrodynamic instability gives birth to a liquid bridge that growths as $R_m \sim t$. This scaling law is characteristic of the Inertially-limited-Viscous regime (ILV) that takes place when $\mathrm{Oh_m} \sim 1$[9,15,16]. In the ILV regime, the experimental contours of the interface in the meridian plane (r,z) of the bridge are well described by a parabola: $z \propto r^2/R$, where R is the radius of the droplets[15]. This result is in agreement with the scaling of Refs 8 and 17. However, as R_m increases, $\mathrm{Oh_m}$ decreases and the central part of the bridge flattens. A transition to an inertial regime is then observed ($\mathrm{Oh_m} \ll 1$). In this regime, all published pictures[9,15,16,18–25] as well as those presented in the following of this article, show that the central part of the bridge adopts a surprising cylindrical shape. The capillary pressure at the connecting points between the cylindrical bridge and the droplets (forming two circles, located at points A_1 and A_2 defined later in fig. 3) is responsible for the bridge expansion with a converging flow which stops at the middle of the bridge[26,27].

For the inertial regime, Ref. 8 proposed the following scaling law by assuming that the driving underpressure is given by $\gamma/(R_m^2/R)$:

$$\frac{R_m}{R} = C_0 \left(\frac{t}{\tau_C}\right)^{1/2}, \tag{1}$$

where $\tau_C = \left(\rho R^3/\gamma\right)^{1/2}$. Later, Ref. 17 solved numerically the expansion by considering an inviscid bridge, neglecting the presence of the outer fluid and initialising the computation with a bridge of length Δ much smaller than its radius and scaling as $\Delta \propto R_m^2/R$. Their results exhibited sequences of formation of a toroidal gas enclosure followed by a reconnection. Nevertheless, the evolution of the bridge radius was found in agreement with the $t^{1/2}$ law as confirmed by numerical simulations[22]. A few experimental studies of the expansion of the liquid bridge after coalescence have been carried out[9,15,16,19–21,28,29]. In the inertial regime, the results are found in good agreement with equation (1), with a prefactor C_0 of order of unity, but with an exact value that depends on the fluid properties. Hence, we recently observed that damped oscillations of the bridge are initiated when inertia dominates until the final equilibrium shape of the two merged droplets is reached[30].

Finally, one can note that the Ohnesorge number is usually defined by considering that the scale of coalescence is given by the droplet radius, $\mathrm{Oh} = \mu/\sqrt{\rho\gamma R}$, which is also the ratio of the square root of the Weber number and the Reynolds number. In this case, the flow regime characteristic of the bridge expansion depends on both R_m/R and Oh, according to Ref. 15. For a given R_m/R, low Oh corresponds always to the inertial regime, large Oh to the viscous regime and intermediate Oh to ILV regime.

The present work focuses on the expansion of the fluid bridge that takes place after the jump to contact between two liquid droplets in air. Here, the objective is to provide a deeper understanding of the dynamics in the inertial regime all along the bridge expansion, from the initial film breakup up to the instant it reaches a size comparable to that of the initial droplets. A series of experiments have been carried out, in which two liquid droplets in air are put into contact at negligible approach velocity until they coalesce. The interface is recorded by high-speed imaging and its contour is determined by video processing. The time evolution of the overall shape of the bridge is analyzed in detail. It is observed that the contact point at the optical scale gives rise to four regions (two on each side) where the slope of the interface can be considered to be discontinuous at this scale. The propagation of non dispersive wave packets, causing a linear evolution of the bridge length with time is responsible of the growth of the initial bridge just after the jump to contact. Moreover,

Bridge expansion after coalescence of two droplets in air

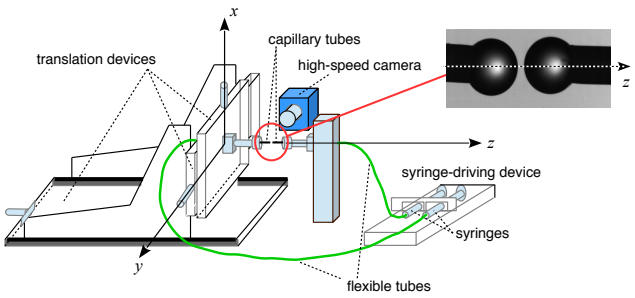

FIG. 1. Schematic of the experimental setup for droplets generation and high-speed imaging.

TABLE I. Physical properties of the liquids, Ohnesorge number and characteristic scales, estimated with R=400 μm. The properties of aqueous solutions of $MgSO_4$ do not significantly differ from those of water.

liquid	ρ (kg/m^3)	γ (N/m)	μ (Pa s)	Oh	τ_C (ms)	τ_{vis} (ms)	U_C(m/s)	U_{vis}(m/s)
water	1.000×10^3	72×10^{-3}	1×10^{-3}	6×10^{-3}	1	6×10^{-3}	0.4	72
PDMS	0.965×10^3	20×10^{-3}	5×10^{-3}	6×10^{-2}	2	0.1	0.2	4.0
paraffin	0.865×10^3	33×10^{-3}	50×10^{-3}	5×10^{-1}	1	0.6	0.3	0.66

we found that the slope discontinuity observed by optical camera determines the rate of the flow entering the bridge and the time evolution of its radius.

The article is organized as follows. The experimental setup and the fluid properties are described in section II. The main features of the bridge shape in the ILV and the inertial regimes are presented in section III. The evolution of the bridge length is analyzed in terms of capillary waves in section IV. The liquid flow through the bridge is interpreted by considering the two-dimensional potential flow in between four dihedrals in section V. Concluding remarks are provided in section VI.

II. EXPERIMENTAL SETUP

The experimental setup is depicted in fig. 1. Two liquid droplets are formed in air at the extremities of two facing horizontal capillary tubes by injecting a liquid by means of a syringe pump. Sixty-five tests have been carried out with droplets of radius ranging between 150 and 510 μm.

Bridge expansion after coalescence of two droplets in air

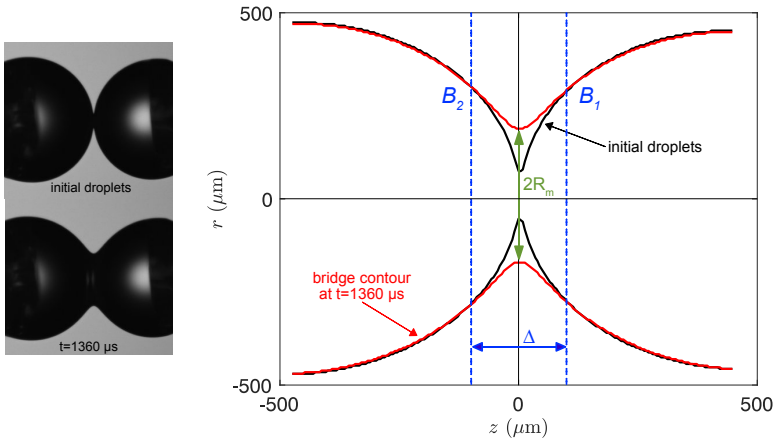

FIG. 2. Shadow images (left) and detected contour (right) of the initial drops and the bridge at t=1360 μs, in the case of two drops of liquid paraffin of the same radius, R=470 μm. The vertical dashed lines passing by points B_1 and B_2 correspond to the limits of the bridge.

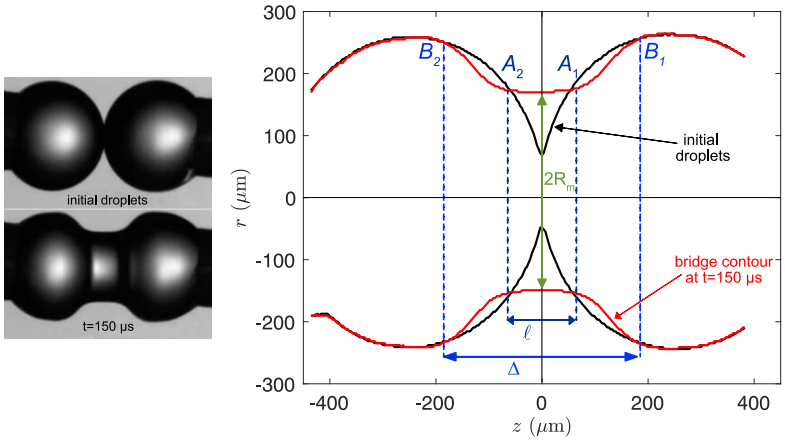

FIG. 3. Shadow images (left) and detected contour (right) of the initial drops and the bridge at t=150 μs, in the case of two water drops of the same radius, R=250 μm. The vertical dashed lines passing by points B_1 and B_2 correspond to the limits of the bridge. The vertical dashed lines passing by points A_1 and A_2 correspond to the limit of the cylindrical part of the bridge, which is present in the inertial regime.

The investigation mainly focuses on systems with two droplets of the same size but radius ratios between 0.65 and 1 have been also considered. The experiments are operated at room temperature ($20 \pm 1^{\circ}$C) and atmospheric pressure. The considered liquids are water (11 tests done), aqueous solutions of manganese sulfate ($MgSO_4$) at various concentrations (0.4 g.L^{-1}: 21 tests; 0.8 g.L^{-1}: 6 tests; or 4 g.L^{-1}: 12 tests) which is known to inhibit coalescence, low viscosity polydimethylsiloxane (PDMS: 10 tests) and liquid paraffin (5 tests). The pump is stopped just before the two drops touch each other. The droplets however continue growing because of the residual excess of pressure in the deformable tubes that supply the liquid from the syringes to the capillaries. This growth is very slow ($< 100\,\mu$L h^{-1}) so that the approach velocity is less than 100 μm s^{-1}. Therefore, the viscous forces associated to the drainage of air in the interstice in between the two droplets are negligible. The droplets remain thus spherical until molecular forces between facing interfaces cause a liquid bridge to form between them.

The capillary tubes, aligned along the horizontal z-direction, are made of PolyEtherEtherKetone (PEEK). Thanks to a three-axis micro-translation system, the distance between the tube extremities is adjusted. Experiments have been conducted with tubes of two different outer radii a equal to $180 \pm 5\,\mu$m or $305 \pm 5\,\mu$m, but with the same inner radius, $25\,\mu$m. It has been checked that the gas-liquid interface remains attached to the outer edge of the capillaries and that the angle it makes with the tube is free to change. The droplets are illuminated by means of a LED backlight. Shadow images of the droplets or the bridge are recorded thanks to a high-speed camera (V1210 Phantom or Photron SA-X2). The acquisition frequency is in between 50000 to 100000 frames per second and the exposure time is around 16 μs. The image size is 512×320 pixels, which approximately corresponds to a visualisation window of 2.5 mm in the axial direction and 1.6 mm in the radial one. Eventually, the spatial resolution δx is $5\,\mu$m/px and the time resolution δt is in between 10–20 μs. In the following, the time origin is defined as the instant of bridge formation, which is determined with an experimental uncertainty of $\pm\delta t$.

Movies of the entire process are recorded for each experimental run. At each instant, the contour of the gas-liquid interface in the vertical symmetry plane (xOz) is detected by standard digital image processing. Examples of images and contours are given in fig. 2 for paraffin droplets and in fig. 3 for water droplets. Before the film rupture (top images on the left and black contours on the right in figs. 2 and 3), the two droplets appear as spheres truncated at their connection to the capillary tubes. In the central part, although they seem to be in contact because of the optical limitations of our system, there are still separated by a very thin film of air, which is thus under

the resolution of our measurements. The very central part of the contours is thus discarded. The part of the contour that is correctly detected turns out be an exact circle, at the resolution of the experiments. The radius, R_1 and R_2 of the two initial droplets can thus be accurately monitored all along the initial growing process, allowing us to determine the approach velocity of the two interfaces. Because the radii of the two droplets can differ, the mean radius, $R = (2R_1R_2)/(R_1+R_2)$, is introduced. Its value at the instant of the film rupture is used to characterize the system. During the coalescence process, we have checked that the droplet radii are unchanged and consequently, that the liquid inside the capillaries do not participate to the bridge expansion. Even though the interstice between the droplets is partly hidden by a disturbing shadow, distinct differences are visible between the image that immediately precedes the film rupture and the image that immediately follows it. The instant of film rupture can thus be unambiguously located in the time interval of duration $\pm\delta$t$\approx$15 μs. For all results presented in this article, the origin of time is taken at the instant corresponding to the last image before the bridge formation. The first contour of the bridge can only be determined after the bridge length has become large enough to emerge from the central disturbing shadow. This occurs a few δt after the film rupture. After the film rupture (bottom images on the left and red contours on the right in figs. 2 and 3), a single interface is formed, which can be decomposed into three regions: a central liquid bridge which grows with time, surrounded by two regions that have not been affected yet by the bridge formation and thus remain exact portions of spheres. As it has already been mentioned in the introduction, the process around the film rupture comprises a first step at the nanoscale involving molecular interactions followed by a bridge expansion at the drop scale that can be fully described as a classic hydrodynamic process. In this work, we focus on this hydrodynamic step with the time and spatial resolutions described above.

The properties of the various liquids are given in Table I together with the Ohnesorge number calculated with the droplet radius and some relevant scales: the capillary-inertial time, $\tau_C = \sqrt{\frac{\rho R^3}{\gamma}}$, and velocity, $U_C = \sqrt{\frac{\gamma}{\rho R}}$, which are characteristic of the inertial regime; the capillary-viscous time, $\tau_{\text{vis}} = \mu R/\gamma$, and velocity, $U_{\text{vis}} = \gamma/\mu$, which are characteristic of the viscous regime. Water and $MgSO_4$ aqueous solutions have similar physical density, viscosity and surface tension. However, adding $MgSO_4$ to water[31,32] is known to inhibit the coalescence of air bubbles. It may therefore affect the coalescence process at the nanoscale and thus change the characteristics of the initial liquid bridge at the scale considered here. With water or $MgSO_4$-water, the Ohnesorge number is very low ($\approx 6\times10^{-3}$) and only the inertial regime can be observed. With PDMS, the viscosity is

Bridge expansion after coalescence of two droplets in air

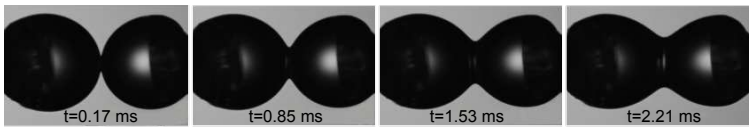

FIG. 4. Typical sequence of bridge expansion in ILV regime, in the case of two liquid-paraffin droplets of same radius 470 μm (same case as fig. 2). The minimum radius is localized at the center of the bridge where the interface shows a smooth parabolic shape.

five times larger but Oh is still low ($\approx 6 \times 10^{-2}$) and we can expect that the expansion is still in the inertial regime. In contrast, with liquid paraffin (Oh$\approx 5 \times 10^{-1}$), viscous effect should not be negligible and a ILV regime is expected.

III. SHAPE AND EXPANSION OF THE LIQUID BRIDGE

In this section we describe the main features of the bridge shape all along its expansion in both the ILV regime and the inertial one.

A. Inertially-Limited-Viscous regime

We begin by considering droplets of liquid paraffin, for which capillary-viscous and capillary-inertial characteristic scales are similar (Table I): $\tau_C \approx \tau_{vis} \approx 1$ ms and $U_C \approx U_{vis} \approx 0.5$ m s^{-1}. The Ohnesorge number is thus of the order of unity and the bridge expansion is expected to belong to the ILV regime. Although the main objective of this work is to focus on the inertial regime, it is interesting to describe the main features of the ILV regime in order to display the contrast that exists between a regime where viscosity does play a significant role in the expansion rate and a regime where it does not.

Figure 4 shows a typical sequence of images of the interface evolution for two paraffin droplets of almost equal size. The geometry of the bridge is characterized by several parameters that are defined on the contour plot in fig. 2. Points B1 and B2 denote the maximal location reached by the disturbance initially generated by the film rupture. They are located by detecting the first location where the deviation of the current contour relative to the initial spherical one is more than one pixel. The central region in between B1 and B2 corresponds to the bridge whereas the interface

Bridge expansion after coalescence of two droplets in air

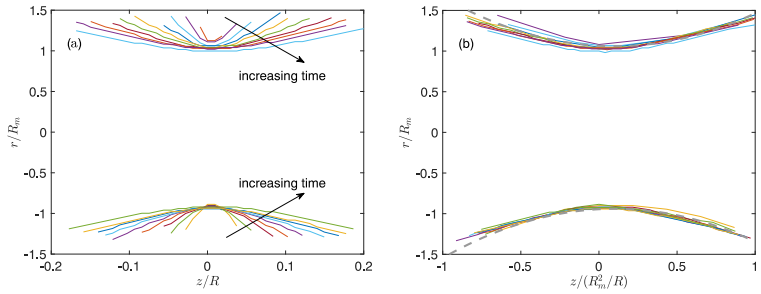

FIG. 5. Successive profiles of the bridge in the case of liquid paraffin (same case as fig. 2). A profile is plotted each ten images ($10\delta t$=170 μs) from t=170 μs to 1820 μs. The radial coordinate r is normalized by R_m. (a), evolving profiles when z is normalized by the droplet radius R; (b), constant parabolic profile when z is normalized by $R_m(t)^2/R$. The dashed light gray curve is an exact parabola for reference purpose. Corresponding values of $R_m(t)$ are plotted in figure 6.

beyond B1 and B2 is still spherical and the same as it was before the film rupture. The length Δ of the bridge is defined as the distance between B1 and B2 along the axial direction z. Its radius R_m is given by half the minimum distance between the two points of the interface along a vertical line. The growth rate of the bridge in each direction is characterized by the time derivative, $\dot{\Delta}$ or $\dot{R}_m$, of these quantities.

Figure 5 shows successive contours of the bridge during its expansion. The approximate parabolic profiles image the effects of viscous dissipation. The region of maximum interface curvature remains located in the middle of the bridge during the whole process. It is responsible for a low pressure that drives the liquid within the bridge and causes its thickening. The contours become independent of time when the radial coordinate is normalized by minimum radius $R_m(t)$ and the axial one by the minimum curvature radius $R_m^2(t)/R$, in agreement with the experiments of Ref. 15 and the scaling proposed by Ref. 8. A unique normalized parabolic profile can be then plotted.

Figure 6 shows the time evolution of the characteristic dimensions of the liquid bridge. Δ and R_m are normalised by R=470 μm while t is normalized by τ_C=1600 μs. Note that the description is provided until both Δ and R_m reach approximately $0.5R$, which means the end of the bridge expansion. We are thus clearly not limiting our analysis to the initial stage of the expansion. The evolution of R_m is linear up to $t_{crit} \approx 0.5\tau_C$, with $\dot{R_m}$=0.11 m/s, to be compared to $U_{vis} = 0.7$ m/s

Bridge expansion after coalescence of two droplets in air

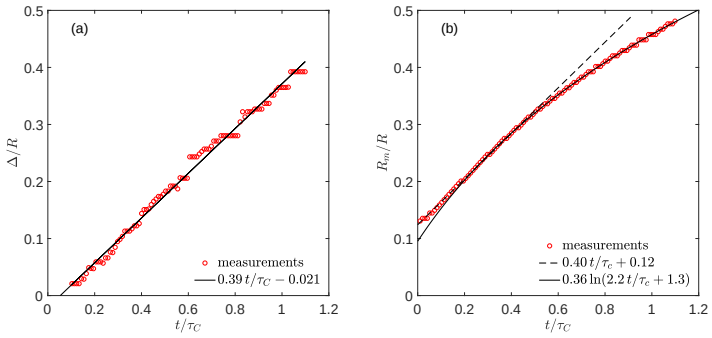

FIG. 6. Time evolution of bridge dimensions in the case of liquid paraffin (same case as fig. 2): (a) bridge length, Δ; (b) bridge radius, R_m.

and $U_C = 0.3$ m/s for this particular droplet size. This first regime thus shows all the characteristics of the ILV regime: constant growth rate of the bridge radius and parabolic shape. At larger times, because the characteristic scale of the flow becomes larger, inertia becomes more important and the evolution of R_m slows down. The velocity $\dot{R}_m$ is thus no longer constant but a same normalized profile is still observed. At variance with R_m, Δ remains a linear function of time all along the process, with a velocity, $\dot{\Delta}$=0.11 m/s, equal to the initial value of $\dot{R_m}$. The transition observed around $0.5\tau_C$, which marks the end of the ILV regime defined by Ref. 15, is thus affecting only R_m, indicating that the axial and the radial dimensions of the bridge are not controlled by the same process. As we shall see in the next section, the linear evolution of Δ is still observed in the inertial regime, which suggests that it may be driven by the same mechanism in both the ILV and the inertial regime.

B. Inertial regime

In this section, we describe the experimental expansion of a bridge resulting from the coalescence of two droplets of water, aqueous solutions of $MgSO_4$ or low viscosity PDMS. No difference in the present results could be seen between solutions of $MgSO_4$ of various concentrations and water. This is consistent with Ref. 15 who did not mentioned any effect of NaCl that was added to water for purpose of performing measurements based on electrical conductivity. If ever the presence of electric charges at the interface affects the coalescence of bubbles in water, it has no

Bridge expansion after coalescence of two droplets in air

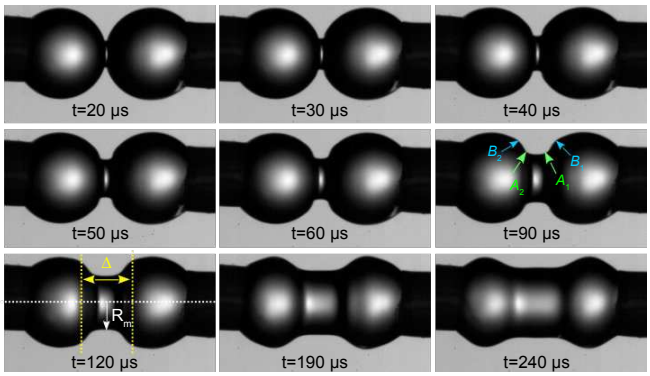

FIG. 7. Typical sequence of bridge expansion, in the case of two identical water droplets of radius 250 μm. (same case as fig. 3). A cylindrical bridge of constant radius connects the two droplets at A_i by making an apparent change of slope.

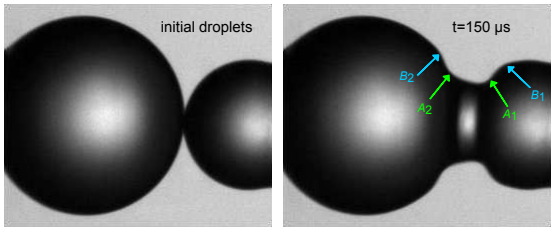

FIG. 8. Coalescence of two water droplets of different size (R_1=310 μm, R_2=200 μm). The central region, deprived of meridian curvature, is a truncated cone.

influence on the dynamics of a liquid bridge in air. In the following, we shall therefore not distinguish between water and water-$MgSO_4$ droplets. On the other hand, comparisons between water (Oh$\approx 6\times10^{-3}$) and PDMS (Oh$\approx 6\times10^{-2}$) droplets are devoted to the detection of a possible low effect of viscosity and the assessment of the limits of the inertial regime.

Figure 7 shows a sequence of images of the bridge expansion after the coalescence of two water droplets of the same size (R=250 μm). In contrast with what is observed with liquid paraffin, the region of maximal interface curvature is split into two parts that move away in opposite directions. The bridge surface thus involves three regions (see notations in fig. 3). The central region is almost deprived of meridian curvature and adopts a cylindrical shape. We define A_1 and A_2 as the points

Bridge expansion after coalescence of two droplets in air

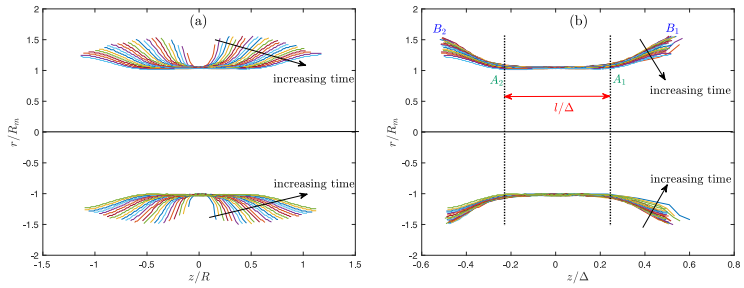

FIG. 9. Successive profiles of the bridge in the case of a water (same case as fig. 3). A profile is plotted for each image (δt=10 μs) from t=50 μs to 280 μs. The radial coordinate r is normalised by R_m. (a), evolving profiles when z is normalized by the droplet radius R; (b), constant cylindrical normalized profile between A1 and A2 when z is normalized by Δ.

of the circles that locate the ending sections of this cylinder. On both sides, in between A_1-B_1 and A_2-B_2, two regions connect the cylindrical part to the parts of the interface that are not yet affected by the coalescence. The transitions between these regions are sharp and the interface curvature at points A_1, A_2, B_1 and B_2 are under the resolution of our measurement technique. These points thus rather appear to us as places of slope discontinuity. The case where the sizes of the two droplets are different is illustrated in fig. 8, where R_2/R_1=0.65. The central part is no longer a cylinder but a truncated cone. It is however still deprived of meridian curvature and lines A_1, A_2, B_1, B_2 are still places of slope discontinuity at the resolved scale. Figure 9 shows the successive contours of the bridge. A unique profile is again observed when r is normalized by $R_m(t)$ and z by $\Delta(t)$, but is it limited to the cylindrical (resp. conical) central part of the bridge for two droplets of the same (resp. different) size. We have measured the length l between A_1 and A_2 in the 50 tests carried out with water or water-$MgSO_4$ droplets and found that $l(t) = [0.53 \pm 0.04]\Delta(t)$.

The same analysis has been done with the 10 tests performed with PDMS droplets. It turns out that the bridge interface shows similar features to the case with water droplets. The only significant difference is that the unique normalized profile is found approximately to be half shorter: $l(t) = [0.28 \pm 0.02]\Delta(t)$.

The shape of the bridge interface having been described, we focus now on its growth rates in both axial and radial directions. Figure 10 shows the time evolution of bridge length Δ and radius R_m in three tests carried out with water droplets of various sizes. Figure 11 shows similar results

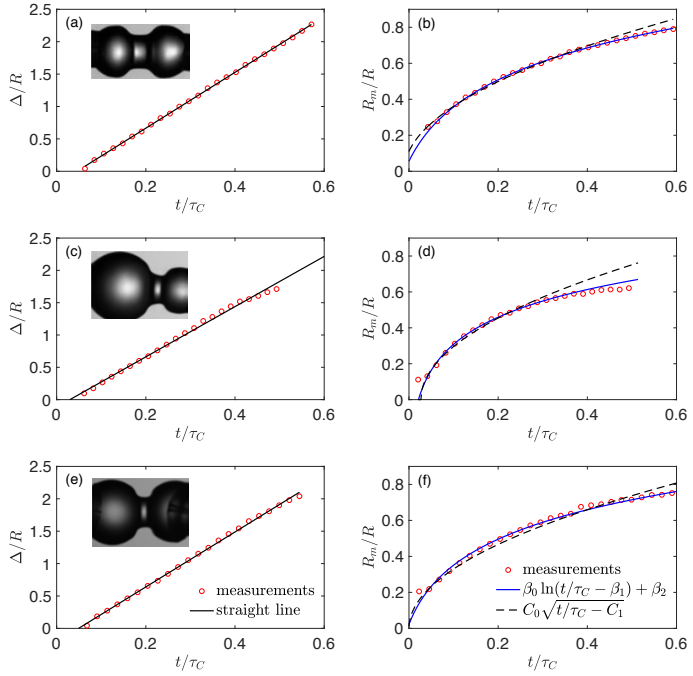

FIG. 10. Time evolution of bridge dimensions, Δ and R_m, of droplets of water or water-$MgSO_4$ of various sizes. (a) and (b), two droplets of the same size (R=R_1=R_2=250 μm, same case as fig. 3); (c) and (d), two droplets of different sizes (R=250 μm, R_1=325 μm, R_2=205 μm); (e) and (f), two droplets of the same size (R=R_1=R_2=340 μm).

for a case with PDMS. In any case, the axial expansion speed $\dot{\Delta}$ is constant all along the process. Figure 12 shows this speed as a function of the capillary-inertial speed U_C for all performed tests. It turns out to be remarkably similar for all tests carried out with water or PDMS, whatever the droplet size: $\dot{\Delta} = [4.2 \pm 0.3]U_C$. In the case of paraffin droplets, the values of $\dot{\Delta}$, also reported in fig. 11, are much smaller: $\dot{\Delta} = [0.5 \pm 0.1]U_C$. In general, the speed of axial expansion thus depends on viscosity. Since the Reynolds number of the liquid flow that enters into the bridge during the expansion increases with time, we should therefore expect $\dot{\Delta}$ to change over time. The fact that water and PDMS cases show similar $\dot{\Delta}$ means that the inviscid limit of this quantity has been

Bridge expansion after coalescence of two droplets in air

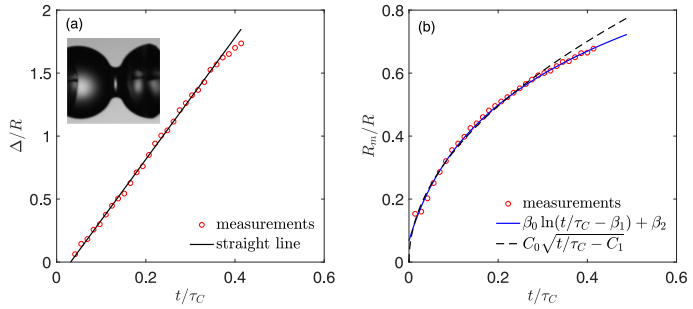

FIG. 11. Time evolution of bridge dimensions, Δ (a) and R_m (b), of two droplets of PDMS of the same size (R=R_1=R_2=315 μm);

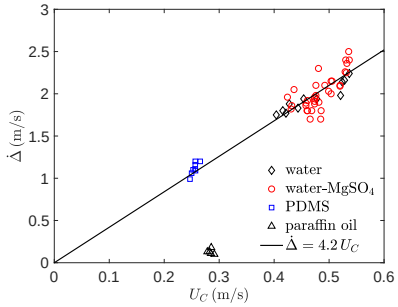

FIG. 12. Growth rate of the bridge length, $\dot{\Delta}$, as a function of the capillary-inertial velocity U_C, for various test conditions.

reached from the beginning of the process. It is therefore not surprising that $\dot{\Delta}$ remains constant during the expansion with these two fluids. However, the length l of the central part also increases at a constant rate whereas its value significantly differs between water ($\dot{l} \approx 2.2\,U_C$) and PDMS ($\dot{l} \approx 1.2\,U_C$). In addition, a constant $\dot{\Delta}$ can hardly be understood in the case of paraffin droplets if the evolution of the bridge length is associated to the bulk liquid flow within the bridge. All together, this suggests that the speed of lines B_1 and B_2 as well as that of A_1 and A_2, are prescribed by capillary waves that only involves a liquid flow in the vicinity of the interface.

The dynamics of the radial expansion of the bridge is different from the axial one, with a growth rate that regularly decreases with time (figs. 10.b,d,e and 11.b). In agreement with previous

TABLE II. Experimental values of prefactor C_0 of eq. 1 for various fluids (average value $\pm$ standard deviation).

	water	methanol	glycerol+water	PDMS 5 mPa s	PDMS 20 mPa s
Ref. 20	1.14			1.24	1.11
Ref. 28	1.09 ± 0.08	1.29 ± 0.05	1.03 ± 0.07		
Present study	1.04 ± 0.07			1.05 ± 0.02	

works (see Table II) and eq. 1, the first stage of the expansion is rather well described by a square root of time, $R_m/R = C_0\sqrt{t/\tau_C - C_1}$. The adjusted time origin C_1 is found to be in the expected interval, between the image just before and the image just after the film rupture. The values of prefactor C_0 obtained in this study are reported in Table II together with those of previous experiments. We found that C_0 is close to unity in all our experimental runs with both water and PDMS cases, which is in agreement with results obtained by Ref. 28 with water or water-glycerol, but slightly smaller than values measured by Ref. 20 with water or PDMS. Furthermore, numerical simulations by Ref. 17 found a larger value, C_0=1.6. Ultimately, we can conclude that the fit in $t^{1/2}$ is the right scaling of the first stage of $R_m(t)$. However, it fails to fit accurately our results over the whole duration of the experimental runs, which are better described by a logarithmic law, $R_m/R = \beta_0 \ln(t/\tau_C - \beta_1) + \beta_2$, with a time origin (given by β_1 and β_2). The best fit is obtained with a prefactor $\beta_0 = 0.26 \pm 0.07$. (Note that the same logarithmic law with a similar value of β_0 fits also well the second regime of $R_m(t)$ observed with paraffine droplets.)

A rather complete description of the dynamics of the interface of the liquid bridge in the inertial regime has been achieved. The next sections are devoted to get a better understanding of the mechanisms that control the growth of the bridge in the axial and radial directions.

IV. DESCRIPTION OF THE INTERFACE DEFORMATION IN TERMS OF CAPILLARY WAVES

Now we consider the entire bridge of liquid that joins the two capillaries separated by a distance L, with the aim to analyze the axial expansion in the inertial regime that is observed for water or PDMS droplets. As discussed above, capillary waves seem to drive the motion of the slope discontinuities and controlling their speed, $\dot{l}/2$ for lines A_1 and A_2, and $\dot{\Delta}/2$ for lines B_1 and B_2.

In order to assess this interpretation, we propose to project the instantaneous shape of the interface onto a basis of orthogonal modes of various wavelengths. A natural choice is to consider the linear eigenmodes of an inviscid liquid cylinder of radius a and length L, which are simply Fourier modes[33]. Note that the final equilibrium shape of the interface is actually not an exact cylinder but adopts a slightly inflated or deflated form, the linear eigenmodes of which are much more complex[30]. However, the differences between these two bases of modes are not of significant importance here, especially since we are dealing with very high deviations from the equilibrium form. We thus assume an axisymmetric interface described by its radial profile, $r(z,t)$, which is attached on both its extremities to the outer edge of the capillary tubes, $r(-L/2,t) = r(L/2,t) = a$, and is symmetric about the middle plane $z = 0$. Then, we introduce the deformation relative to a cylinder, $\eta(z,t) = r(z,t) - a$. By considering that η is periodic function of z with a period $2L$, the amplitudes of the modes are

$$a_n(t) = \frac{2}{L}\int_{-L/2}^{L/2} \eta(z,t)\cos(k_n z)\,dz, \tag{2}$$

with

$$k_n = \frac{n\pi}{L}, \tag{3}$$

and the spatial profile can be written

$$\eta(z,t) = \sum_{n=0}^{\infty} a_n(t)\cos(k_n z)\,. \tag{4}$$

At each instant, the a_n are computed from the experimental data by using eq. 2 and the spatial profile $\eta(z,t)$ reconstructed by using eq. 4 is compared to the experimental one. In any case, limiting the expansion to $n = 40$ was enough to match the experimental shape within the measurement accuracy. Figure 13 shows the amplitude $|a_n|$ of the modes as a function of the mode order n, at various instants t, for water droplets. For $n > 5$, we observe that these spectra globally decrease as k_n^{-2}, which is known to be the signature of discontinuities of slope[34,35]. The presence of the slope discontinuities at A_1, A_2, B_1 and B_2 is thus dominating the evolution of the spectrum at large wavenumbers.

Then, the time evolution of each a_n is approximated as a damped harmonic oscillation

$$a_n^0 e^{-\beta_n t}\cos(\omega_n t + \phi_n)\,, \tag{5}$$

where the initial amplitude a_n^0, the frequency ω_n, the damping coefficient β_n and the phase ϕ_n are adjusted in order to provide the best fit of the experimental amplitudes of the modes. Figure 14

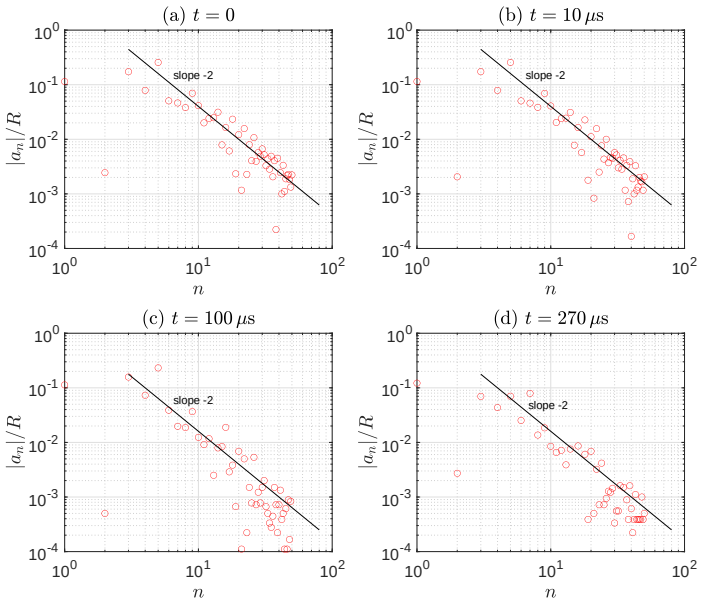

FIG. 13. Wave Spectra: mode amplitudes $|a_n|$ as a function of the mode order n at various instants t for two water-$MgSO_4$ droplets: $t = 0$ (a), $t = 10\mu$s (b), $t = 100\mu$s (c), $t = 270\mu$s (d) (same case as in fig. 3).

shows the time evolution of a few a_n for water-$MgSO_4$ droplets, while fig. 15 presents similar results for the case of PDMS droplets. The fitting curves given by eq. 5 are in reasonably good agreement with the measurements, which indicates that we can interpret each mode as a propagating wave of angular frequency ω_n and wavenumber k_n.

The main plots in fig. 16 display the dispersion relation, $\omega_n = f(k_n)$, of such waves, for water-$MgSO_4$ droplets and PDMS ones. (The results of the PDMS case are only shown until n=20 because the mode amplitude is too small to allow an accurate determination beyond.) Here, the frequency is normalized by $\pi U_C/L$ and plotted against the mode order, $n = k_n L/\pi$, so that the slope corresponds to the group velocity,

$$v_g(n) = \frac{d\omega_n}{dk_n}, \tag{6}$$

normalized by the capillary-inertial velocity, U_C. The insets present the phase velocity,

$$v_\phi(n) = \frac{\omega_n}{k_n}, \tag{7}$$

Bridge expansion after coalescence of two droplets in air

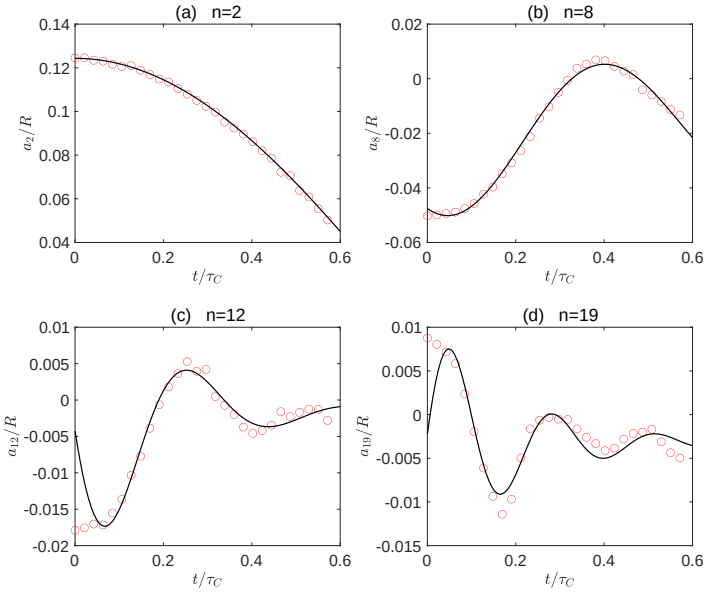

FIG. 14. Time evolution of the amplitude a_n of a few modes for two water-$MgSO_4$ droplets: $n = 2$ (a), $n = 8$ (b), $n = 12$ (c), $n = 19$ (d) (same case as fig. 3). Symbols, amplitudes calculated from experimental profiles by using eq. 2; lines, fitting curves obtained by using eq. 5.

also normalized by U_C and plotted against n. Regarding modes of smaller wavenumbers, the phase velocity regularly increases from 0.7 to 1.5 U_C when n increases from 1 to 10, while the group velocity follows a similar trend but stops increasing sooner, around n=5. Beyond n=10, both $v_g(n)$ and $v_\phi(n)$ are remarkably constant and equal, with a value of about 1.5 U_C, in between $\dot{l}/2$ ($0.6U_C$ for PDMS, $1.1\,U_C$ for water) and $\dot{\Delta}/2$ ($2.1U_C$ for both fluids). The waves of larger wavenumbers, are thus non-dispersive and travel at a speed that is controlled by the capillary-inertial velocity U_C. This is quite surprising since capillary waves are known to be dispersive. First, it is important to note that this result is not related to the basis of modes that is used here. Indeed, if all modes travel at the same speed, projecting them onto another basis conserves this property. Then, we have to remember that the magnitude of the interface deformation is of the same order as the initial droplet radius, R, or the final cylinder radius, a. Moreover, the radius of curvature at the locations of slope discontinuities is very small. We are therefore dealing with modes of large amplitude and thus

Bridge expansion after coalescence of two droplets in air

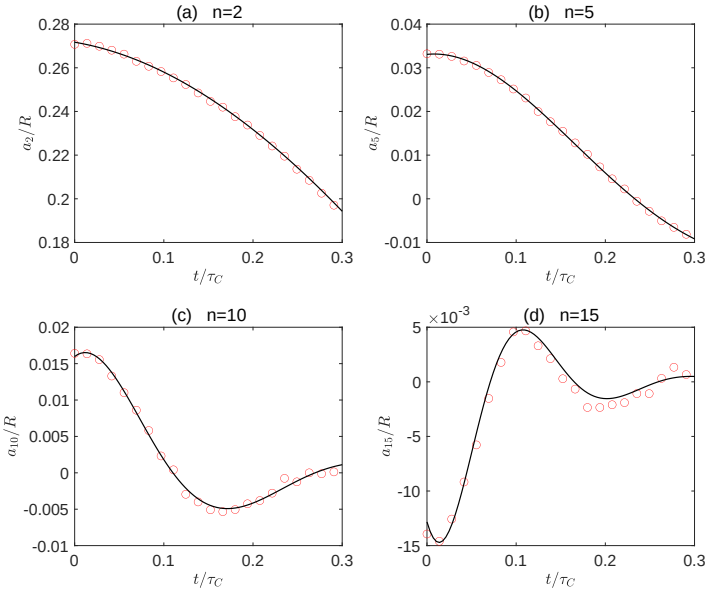

FIG. 15. Time evolution of the amplitude a_n of a few modes for two PDMS droplets: $n = 2$ (a), $n = 5$ (b), $n = 10$ (c), $n = 15$ (same case as fig. 11). Symbols, amplitudes calculated from experimental profiles by using eq. 2; lines, fitting curves obtained by using eq. 5.

with strongly non-linear waves. As in the case of solitons, non-linearities may be responsible for the existence of non-dispersive wave packets.

Even if viscosity does not influence the wave velocity, it may cause wave attenuation. Figure 17 shows the normalized damping rate as a function of n for the same cases as in fig 16. The damping coefficients, β_n/ω_n, are also plotted within the insets. The damping rate is negligible for modes of smaller wavenumbers ($n < 5$), it then increases with n until it reaches a plateau for $n > 20$. As a consequence, the damping coefficient reaches a maximum value, about 0.3 with water and 0.6 with PDMS, for n somewhere between 5 to 25, and then decreases for larger n. The fact that the damping rate saturates at large wavenumbers is consistent with the fact that the shape discontinuities generated by the coalescence of the two droplets can persist until the end of the bridge expansion.

The analysis of the evolution of the bridge interface in terms of capillary waves leads us to

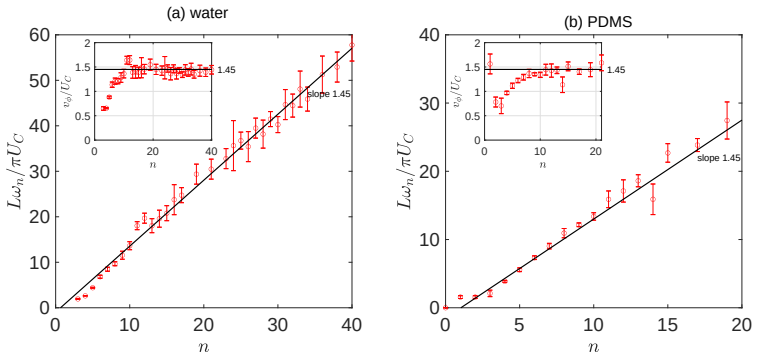

FIG. 16. Dispersion relation of capillary waves. (a), typical example with water-$MgSO_4$ (same case as fig. 3); (b), typical example with PDMS (same case as fig. 11). Main figures: normalized frequency against the normalized wavenumber. Insets: normalized phase velocity against the normalized wavenumber.

the following interpretation. The slope discontinuities located at lines A_i and B_i is characterized by wavenumbers evolving as k^{-2}. They travel as non-dispersive weakly-damped wave packets resulting from a non-linear dynamical process. Since it describes the entire bridge shape, our wave decomposition does not allow us to distinguish between the velocity of lines A_i and B_i. Lines A_i move at the velocity of the slowest waves, which corresponds to wavenumbers $n < 10$, since the interface is flat upstream of them. Lines B_i move at the velocity of the fastest waves, which corresponds to wavenumbers $n \geq 10$, since the interface is not yet influenced by the coalescence downstream of them.

V. HYDRODYNAMIC MODEL

In the previous section, we described the longitudinal expansion of the bridge by considering capillary waves involving only a flow of liquid in the vicinity of the interface. Such an interpretation is relevant only if the flow of liquid within the whole bridge is consistent with the observed evolution of the interface in both the radial and longitudinal directions. Specifically, the liquid flow must satisfy the three requirements listed below.

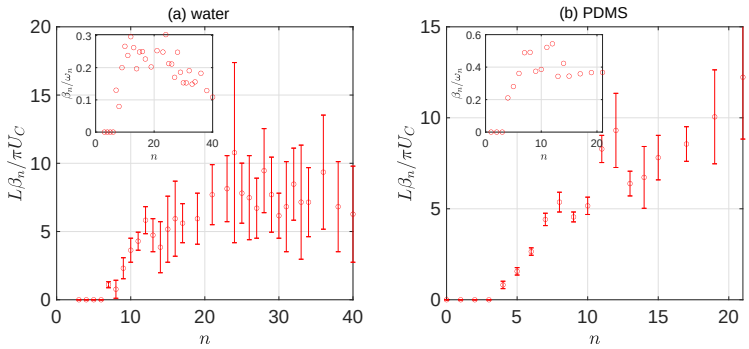

FIG. 17. Damping of capillary waves. (a), typical example with two water-$MgSO_4$ droplets (same case as fig. 3); (b), typical example with two PDMS droplets (same case as fig. 11). Main figures: normalised damping rates against the normalized wavenumber. inset: damping coefficient against the normalized wavenumber.

(i) *Kinematic condition*. The radial liquid velocity v_r has to remain constant along the interface between A_1 and A_2, so as to maintain the cylindrical shape over time,

$$\frac{\partial v_r}{\partial z}(r = R_m, z) = 0 \ \text{ for } z \in [-l/2, l/2]\,. \tag{8}$$

(ii) *Dynamic condition*. The liquid pressure P has also to remain constant along the interface in the central part of the bridge, so that the Laplace's pressure jump across the interface imposes a cylindrical shape,

$$\frac{\partial P}{\partial z}(r = R_m, z) = 0 \ \text{ for } z \in [-l/2, l/2]\,. \tag{9}$$

(iii) *Quantitative agreement*. The computed value of R_m must match experiment.

Solving the complete hydrodynamic problem involving both the liquid flow and the interface deformation can be done by direct numerical simulations. However, it is out of the scope of the present work. In order to understand the nature of flow, we consider a simple model of an inviscid liquid in the simplified two-dimensional plane geometry represented in fig. 18a, which has the same main features as the actual one: symmetric about planes $r = 0$ and $z = 0$, with an interface involving a central part of zero curvature and having discontinuities of slope at points A_{1-4}.

Bridge expansion after coalescence of two droplets in air

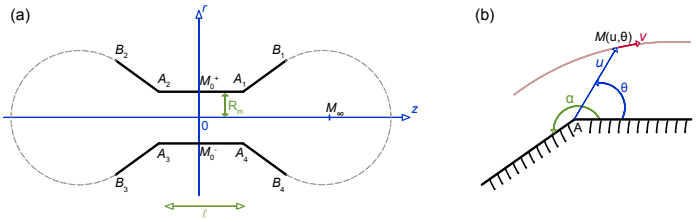

FIG. 18. Schematic of the simplified bridge geometry. (a), whole bridge modelled by four dihedrals; (b) single dihedral.

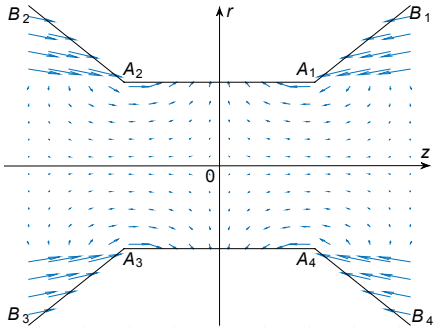

FIG. 19. Example of computed velocity field.

Moreover, we limit our description of the flow to the region within points B_{1-4} and assume that the interface in between points A_i and B_i coincides with a straight line. Thus, we can describe the flow as the superimposition of the four elementary potential flows past the four dihedrals $M_0^+A_1B_1$, $M_0^+A_2B_2$, $M_0^-A_3B_3$ and $M_0^-A_4B_4$ (see fig. 18). Such a superimposition is relevant since potential flows are linear. It is a first order approximation that respects all the geometric symmetries, but does not exactly fulfil the non-penetration boundary condition at the interface.

With the notations defined in fig. 18b, the potential of the flow in a single dihedral of corner A_i is[36],

$$\Phi_{dihedral}(u,\theta) = C\,u^{m+1}\cos\left((m+1)\theta\right), \tag{10}$$

Bridge expansion after coalescence of two droplets in air

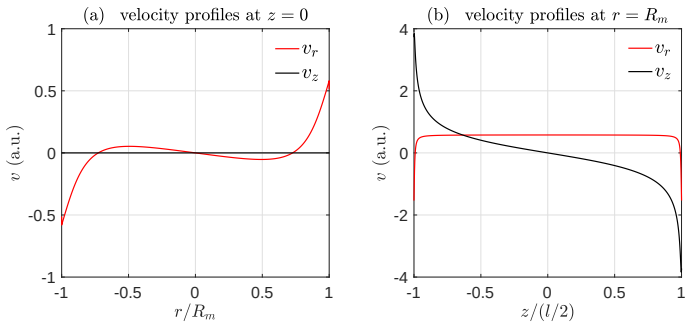

FIG. 20. Profiles of longitudinal and radial velocities in the cylindrical part of the bridge. (a), radial profiles in the center of the bridge at $z = 0$; (b), longitudinal profiles along the interface at $r = R_m$.

and the velocity field is given by,

$$v_u(u,\theta) = C(m+1)u^m \cos\left((m+1)\theta\right), \tag{11}$$

$$v_\theta(u,\theta) = -C(m+1)u^m \sin\left((m+1)\theta\right), \tag{12}$$

$$\tag{13}$$

where $m = \pi/\alpha - 1$, which is comprised between -1 and 0, accounts for the dihedral angle α, and C fixes the magnitude of the incoming velocity. Note that, according to eq. 10, the velocity and the pressure diverge at the corner point A. However, the flow-rate past the corner is finite and the flow is regular on any streamline passing at a finite distance ε from the interface. We can therefore obtain a physically meaningful approximation of the real flow by replacing the sharp boundary by such a streamline. The value of the shifting distance ε would then determine the value of the maximal curvature of the interface. This curvature being under our experimental resolution, it is consistent to keep with a model involving a sharp edge.

After summation of the flows within the four dihedrals centered on each A_i, we get an analytical velocity potential,

$$\Phi_{bridge} = f(\alpha, l, R_m, C), \tag{14}$$

which depends on four parameters: the angle of the dihedrals, α; the length, l, of the central part of the bridge; the radius of the bridge, R_m; the flow parameter, C. Figure 19 presents an example of corresponding velocity field, while fig. 20 displays profiles of both the longitudinal and the radial velocities within the cylindrical part of the bridge. In the middle plane $z = 0$ (fig. 20a), the

Bridge expansion after coalescence of two droplets in air

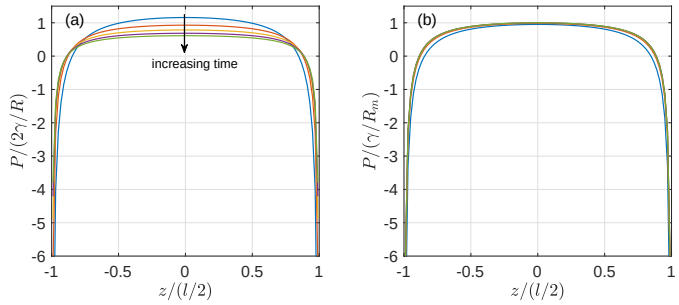

FIG. 21. Pressure profiles along the interface in the cylindrical part of the bridge for two water-$MgSO_4$ droplets (same case as fig. 3), at various instants regularly distributed between 0.13 and 0.55 τ_C. (a), computed pressure normalized by its value in the initial droplet, $2\gamma/R$; (b), computed pressure normalized by its value at the center of the bridge, $\gamma/R_m(t)$.

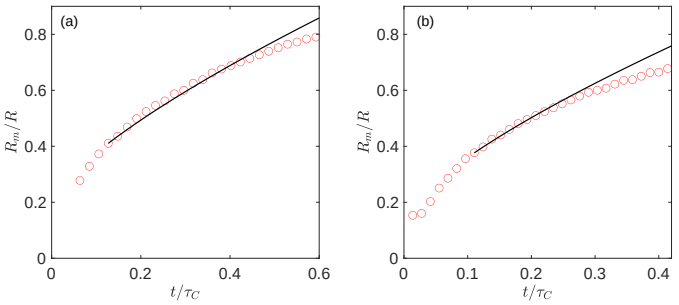

FIG. 22. Computed evolutions of the bridge radius compared to experimental results. (a) water-$MgSO_4$ droplets (same case as fig. 3); (b), PDMS droplets (same case as fig. 11).

longitudinal velocity v_z is zero by symmetry and the radial velocity v_r is only significant in the vicinity of the interface. Along the interface between points A_2 and A_1, the profile of v_z reflects the convergence of the flows that enter by the two opposite sides of the bridge whereas that of v_r is flat excepted very close to points A_2 and A_1, where it diverges. The divergence of the flow is confined to a narrow region around the corners. Therefore, we can conclude that the potential flow in between the four dihedrals satisfies kinematic condition (i) expressed by eq. 8.

Equation 14 determines the liquid flow within a bridge of a given geometry. Now, we have

to determine how the four parameters of Φ_{bridge} evolve in time. In the experiments, the dihedral angle only varies by about 10%, so we will keep it constant and equal to its average value, $\alpha = 4\pi/3$ ($m = -0.25$). The three last parameters are considered as unknowns, which requires three additional equations to be determined. Based on the conclusions of section IV, the longitudinal motion of points A_i is considered to result from a constant speed wave packet,

$$\dot{l} = \kappa U_C, \tag{15}$$

with $\kappa = 2.2$ for water and $\kappa = 1.2$ for PMDS. The second equation expresses that the fluid velocity at the interface must be the same as the interface velocity at point M_0,

$$v_r(M_0) = \left(\frac{\partial \phi_{bridge}}{\partial r}\right)_{M_0} = \dot{R}_m\,. \tag{16}$$

The third equation is the dynamic condition given by the Bernoulli theorem, written between point M_0 located at the interface and a point M_∞ located in the region where the interface is still undeformed and the fluid is at rest,

$$\left(\frac{\partial \Phi_{bridge}}{\partial t}\right)_{M_0} + \frac{\dot{R}_m^2}{2} + \frac{P(M_0)}{\rho} = \frac{P(M_\infty)}{\rho}\,, \tag{17}$$

where the pressures are given by the Laplace's pressure jumps through the gas-liquid interface, which is cylindrical at M_0 and spherical at M_∞,

$$P(M_0) = P_{atm} + \frac{\gamma}{R_m}\,, \tag{18}$$

$$P(M_\infty) = P_{atm} + \frac{2\gamma}{R}\,. \tag{19}$$

The atmospheric pressure, P_{atm}, is taken equal to zero without lost of generality. The non-linear differential systems defined by eqs. 14-19 is solved numerically by using initial values of l, R_m and $\dot{R}_m$ taken from the experiments at the first instant the self-similar cylindrical evolution is well established, $t_{self} \approx 0.1\,\tau_C$. Since the model geometry is symmetric about the plane $z = 0$, only the cases with two droplets of same size are considered.

Let us now examine the predictions of this model. Figure 21 presents pressure profiles along the interface computed at various instants for two water-$MgSO_4$ droplets. Note that positive values correspond to an excess of pressure in the liquid relative to the gas. The negative under pressure compared to P_{atm} in the vicinity of the corners ($z = \pm l/2$) causes the liquid to enter the cylindrical part of the bridge. However, moving away from the corner to the center of the bridge, the pressure

strongly increases and quickly reaches a plateau of positive pressure, which is responsible for the radial expansion of the bridge. In fig. 21a, the pressure is normalized by $P(M_\infty)$, the value within the part of the droplet that is still undeformed. We see that, as time increases, R_m increases and the plateau pressure decreases. In fig. 21b, the pressure is normalized by the value it takes in the middle of the bridge. It turns out that $P/P(M_0)$ quickly reaches a constant profile, which is consistent with the evolution of the bridge. More importantly, this flat profile satisfies dynamic condition (ii) expresses by eq. 9.

Figure 22 compares the computed evolution of R_m with experimental results, which allows us to check condition (iii). We observe a satisfactory agreement between the computed values and the experimental data in the range from t_{self}=0.12 to t_{max}=0.45 τ_C for water-$MgSO_4$ droplets (fig. 22a), and from t_{self}=0.11 to t_{max}=0.30 τ_C for PDMS droplets (fig. 22b). In the final stage of the process ($t > t_{max}$), when Δ becomes comparable to R, there probably exists no more region where the fluid is at rest. Using $2\gamma/R$ as the upstream pressure in the application of the Bernoulli theorem (eq 17) is thus expected to lead to an overestimation of $\dot{R}_m$. All in all, the agreement with the experimental results is quite good considering the crude assumptions made: two-dimensional plane geometry, neglect of vorticity in the vicinity of the corners, approximated flow potential. It is at least sufficient for the present purpose, which was not to provide a predictive model of the bridge expansion, but to confirm our interpretation of the physical mechanisms.

VI. CONCLUSION

We carried out experimental investigations of the coalescence of two liquid droplets in air. We considered droplets of a few hundred micrometers in size and examined situations in which inertia plays an important role. When two droplets are approached at negligible velocity, they remain spherical until the distance between their interfaces reaches a few nanometers. Then, a liquid bridge spontaneously forms between them by jump-to-contact instability due to the action of attractive molecular forces and the coalescence occurs. In this work, we focussed on the dynamics of the expansion of the liquid bridge, from its formation, until it reaches a size comparable to the droplet size. In particular, we paid attention to the persistence of the initial mechanisms of coalescence, the general features of the interface shape and the rate of increase of the minimum radius of the bridge, R_m, as well as that of its longitudinal dimension, Δ. From this analysis, we discuss the physical mechanisms, which are very different depending on the magnitude of viscous

forces relative to inertia, characterized by the Ohnesorge number, Oh.

When Oh is of the order of unity, the initial flow is rapidly attenuated and the interface adopts a parabolic shape of negative curvature. As a consequence, the pressure in the liquid is lower than that in the outer gas and minimum at the bridge center. Capillary forces thus continuously drive liquid into the bridge and causes its expansion. In the longitudinal direction, the expansion rate $\dot{\Delta}$ is constant all along the process while, in the radial direction, $\dot{R}_m$ is constant during the first half of the process but then slows down.

On the other hand, when Oh is small, the region of maximum interface curvature does not remain located at the bridge center. It splits into two meridian lines, passing respectively by points A_1 and A_2 (defined in fig. 3), which move away from the center at constant velocity. The liquid is driven from the droplets to the bridge by the minimum pressure that exists near lines A_i, due to capillarity. However, the liquid flow-rate is not controlled by the value of the curvature at lines A_i, but is determined by the magnitude of sudden slope variation of the interface that takes place around each A_i. The flow around the A_i can thus be modelled as the potential flow within a dihedral. Regarding the liquid flow, lines A_i can thus be seen as locations where takes place a discontinuity of slope. The central part of the bridge, between A_1 and A_2, adopts a cylindrical shape of positive curvature. In this region, capillary pressure is therefore no longer the driving force and the flow continues to move towards the centre of the bridge under the action of inertia. The longitudinal evolution of the bridge can be examined by considering either the distance Δ between extremities B_1 and B_2 of the whole bridge (defined in fig. 3) or the distance l between the extremities A_1 and A_2 of its cylindrical central part. Both increase at a constant velocity, which is proportional to the capillary-inertial velocity U_C. Based on the analysis of the interface dynamics in terms of Fourier modes, we show that lines A_i and B_i of high interface curvature move as non-linear packets of non-dispersive capillary waves. Then, the radial expansion is determined by the potential flow entering, through a converging section of discontinuous slope, into a fluid cylinder of growing length, under the pressure difference between the initial droplets and the middle of the bridge.

ACKNOWLEDGMENTS

The authors thank the federation FERMAT for technical support and gratefully acknowledge S. Cazin for his help in image acquisition and processing.

DATA AVAILABILITY STATEMENT

The data that supports the findings of this study are available within the article.

REFERENCES

[1]H. R. Pruppacher and J. D. Klett, *Microphysics of Clouds and Precipitations* (Springer, 2010).

[2]T. Tadros, *Emulsions: Formation, Stability, Industrial Applications* (De Gruyter, 2016).

[3]J. C. Bird, W. D. Ristenpart, A. Belmonte, and H. A. Stone, "Critical Angle for Electrically Driven Coalescence of Two Conical Droplets," Physical Review Letters **103**, 164502 (2009).

[4]C. T. Bartlett, G. A. Généro, and J. C. Bird, "Coalescence and break-up of nearly inviscid conical droplets," Journal of Fluid Mechanics **763**, 369–385 (2015).

[5]H. Deka, G. Biswas, S. Chakraborty, and A. Dalal, "Coalescence dynamics of unequal sized drops," Physics of Fluids **31**, 012105 (2019).

[6]M. M. Rahman, W. Lee, A. Iyer, and S. J. Williams, "Viscous resistance in drop coalescence," Physics of Fluids **31**, 012104 (2019).

[7]A. K. Chesters, "The modelling of coalescence processes in fluid-liquid dispersions: a review of current understanding," Chem. eng. res. Des. **69**, 259–270 (1991).

[8]J. Eggers, J. Lister, and H. Stone, "Coalescence of liquid drops," J. Fluid Mech. **401**, 293–310 (1999).

[9]J. D. Paulsen, J. C. Burton, S. R. Nagel, S. Appathurai, M. T. Harris, and O. A. Basaran, "The inexorable resistance of inertia determines the initial regime of drop coalescence," Proc. Natl Acad. Sci. USA **109**, 6857–6861 (2012).

[10]C. R. Anthony, M. T. Harris, and O. A. Basaran, "Initial regime of drop coalescence," Phys. Rev. Fluids **5**, 033608 (2020).

[11]C. Mortagne, V. Chireux, R. Ledesma-Alonso, M. Ogier, F. Risso, T. Ondarçuhu, D. Legendre, and P. Tordjeman, "Near-field deformation of a liquid interface by atomic force microscopy," Phys. Rev. E **96**, 012802 (2017).

[12]V. Chireux, M. Protat, F. Risso, T. Ondarçuhu, and P. Tordjeman, "Jump-to-contact instability: The nanoscale mechanism of droplet coalescence in air," Phys. Rev. Fluids **3** (2018).

[13]R. Ledesma-Alonso, D. Legendre, and P. Tordjeman, "Nanoscale deformation of a liquid surface," Phys. Rev. Lett. **108**, 106104 (2012).

[14]R. Ledesma-Alonso, P. Tordjeman, and D. Legendre, "Multiscale deformation of a liquid surface in interaction with a nanoprobe," Phys. Rev. E **85**, 061602 (2012).

[15]J. D. Paulsen, "Approach and coalescence of liquid drops in air," Phys. Rev. E **88**, 063010–1–063010–13 (2013).

[16]X. Xia, C. He, and P. Zhang, "Universality in the viscous-to-inertial coalescence of liquid droplets," Proc. Natl Acad. Sci. USA **116**, 23467–23472 (2019).

[17]L. Duchemin, J. Eggers, and J. Josserand, "Inviscid coalescence of drops," J. Fluid Mech. **487**, 167–178 (2003).

[18]A. Menchaca-Rocha, A. Martínez-Dávalos, R. Núñez, S. Popinet, and S. Zaleski, "Coalescence of liquid drops by surface tension," Phys. Rev. E **63**, 046309 (2001).

[19]S. T. Thoroddsen, K. Takehara, and T. G. Etoh, "The coalescence speed of a pendent and a sessile drop," J. Fluid Mech. **527**, 85–114 (2004).

[20]D. Aarts, H. Lekkerkerker, H. Guo, G. Wegdam, and D. Bonn, "Hydrodynamics of Droplets Coalescence," Phys. Rev. Lett. **95**, 164503–1–164503–4 (2005).

[21]J. D. Paulsen, R. Carmigniani, A. Kannan, J. C. Burton, and S. R. Nagel, "Coalescence of bubbles and drops in an outer fluid," Nat. Commun. **5**, 1–7 (2014).

[22]L. Baroudi, M. Kawaji, and T. Lee, "Effects of initial conditions on the simulation of inertial coalescence of two drops," Comput. Math. Appl. **67**, 282–289 (2014).

[23]J. E. Sprittles and Y. D. Shikhmurzaev, "A parametric study of the coalescence of liquid drops in a viscous gas," J. Fluid Mech. **753**, 279–306 (2014).

[24]J. E. Sprittles and Y. D. Shikhmurzaev, "Dynamics of liquid drops coalescing in the inertial regime," Phys. Rev. E **89**, 063008 (2014).

[25]N. E. Ersoy and M. Eslamian, "Capillary surface wave formation and mixing of miscible liquids during droplet impact onto a liquid film," Physics of Fluids **31**, 012107 (2019).

[26]J. E. Sprittles and Y. D. Shikhmurzaev, "Coalescence of liquid drops: Different models versus experiment," Phys. Fluids **24**, 122105 (2012).

[27]Y. Yoon, F. Baldessari, H. D. Ceniceros, L. G. Leal, and 2007, "Coalescence of two equal-sized deformable drops in an axisymmetric flow," Phys. Fluids **19**, 102102 (2007).

[28]M. Wu, T. Cubaud, and C.-M. Ho, "Scaling law in liquid drop coalescence driven by surface tension," Phys. Fluids **16**, L51–L54 (2004).

[29]J. D. Paulsen, J. C. Burton, and S. R. Nagel, "Viscous to Inertial Crossover in Liquid Drop Coalescence," Phys. Rev. Lett. **106**, 114501 (2011).

[30]V. Chireux, D. Fabre, F. Risso, and P. Tordjeman, "Oscillations of a liquid bridge resulting of the coalescence of two droplets," Phys. Fluids **27** (2015).

[31]K.-H. Tsao and D. L. Koch, "Collisions of slightly deformable, high Reynolds number bubbles with short-range repulsive forces," Phys. Fluids **6**, 2591–2625 (1994).

[32]E. Bouche, V. Roig, F. Risso, and A. Billet, "Homogeneous swarm of high-Reynolds-number bubbles rising within a thin gap. Part 1. Bubble dynamics," J. Fluid Mech. **704**, 211–231 (2012).

[33]H. Lamb, *Hydrodynamics*, 6th ed. (Cambridge University Press, 1932).

[34]C. M. Harris, "Exploring smoothness and discontinuities in human motor behaviour with Fourier analysis," Math. Biosci. **188**, 99–116 (2004).

[35]F. Risso, "Theoretical model for k^{-3} spectra in dispersed multiphase flows," Phys. Fluids **23**, 011701–4 (2011).

[36]E. Guyon, J.-P. Hulin, and L. Petit, *Hydrodynamique Physique* (EDP Sciences - CNRS Editions, 2001).

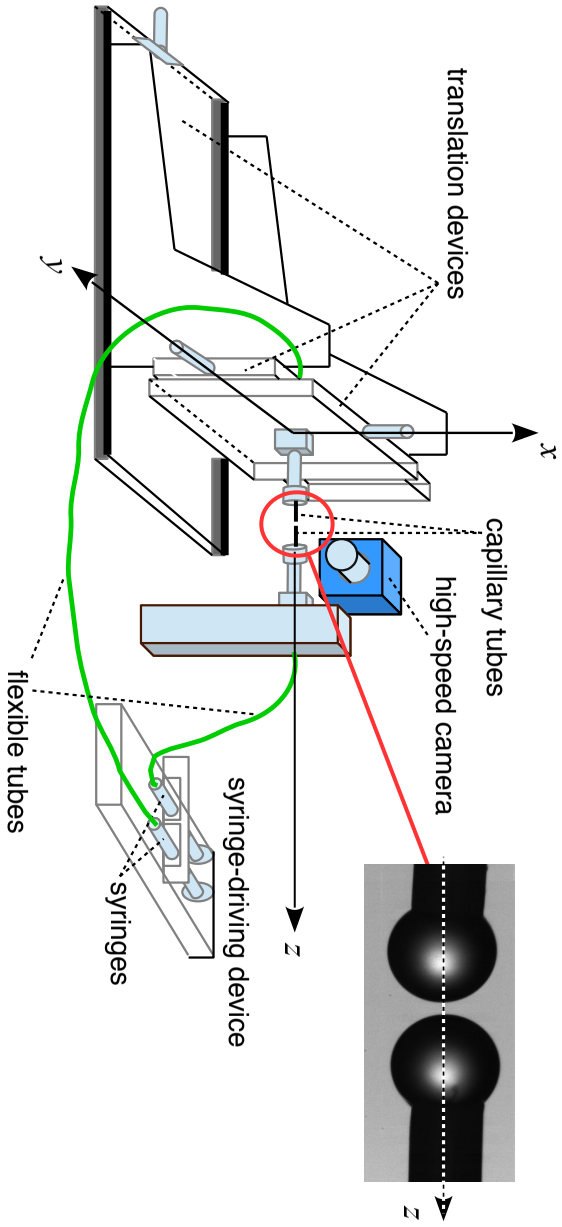

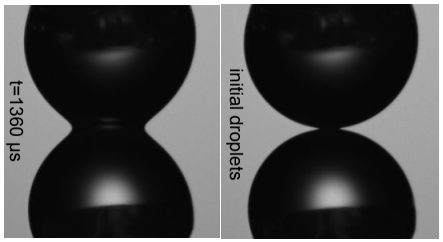

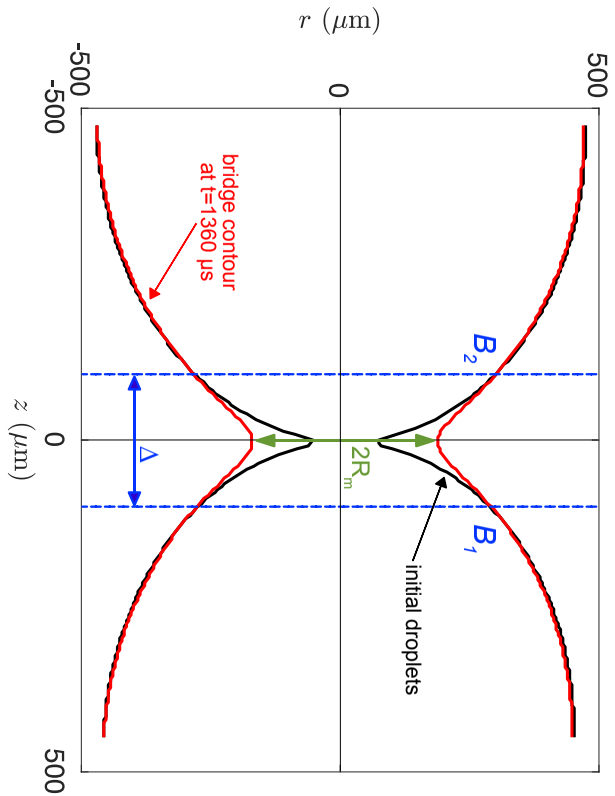

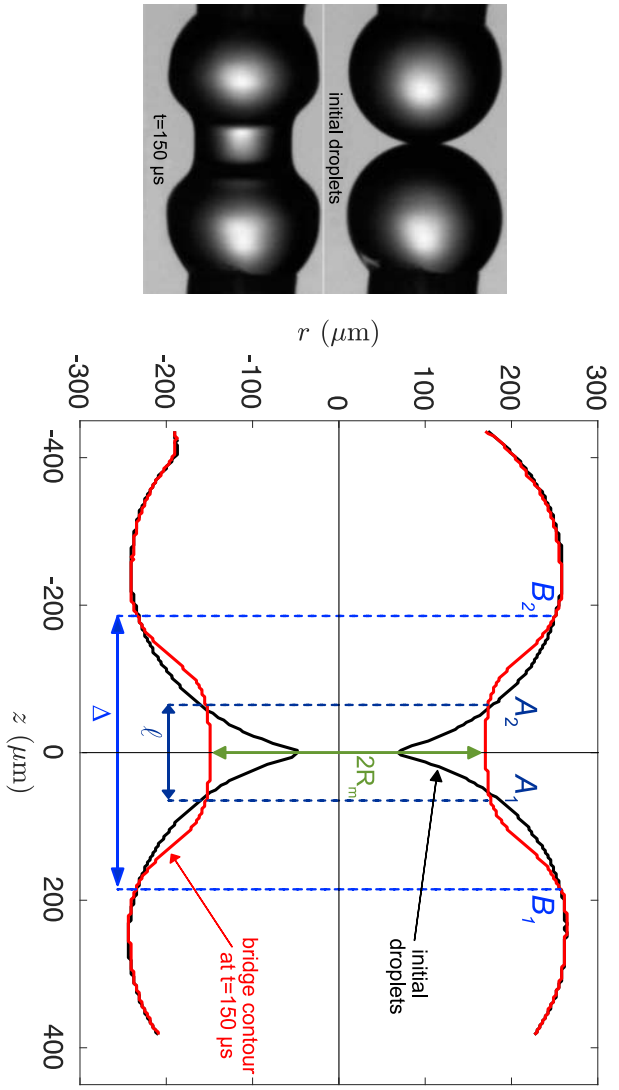

PLEASE CITE THIS ARTICLE AS DOI: 10.1063/5.0055238

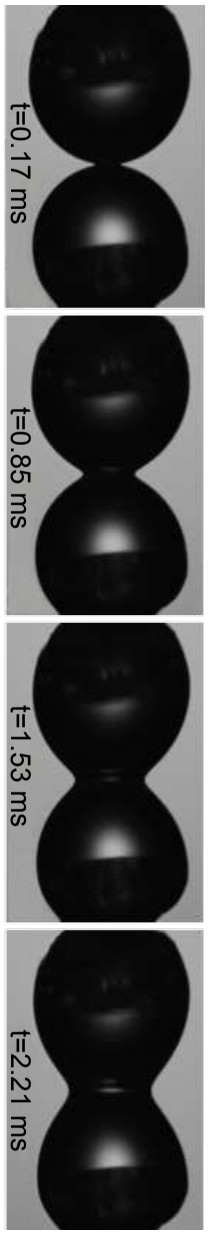

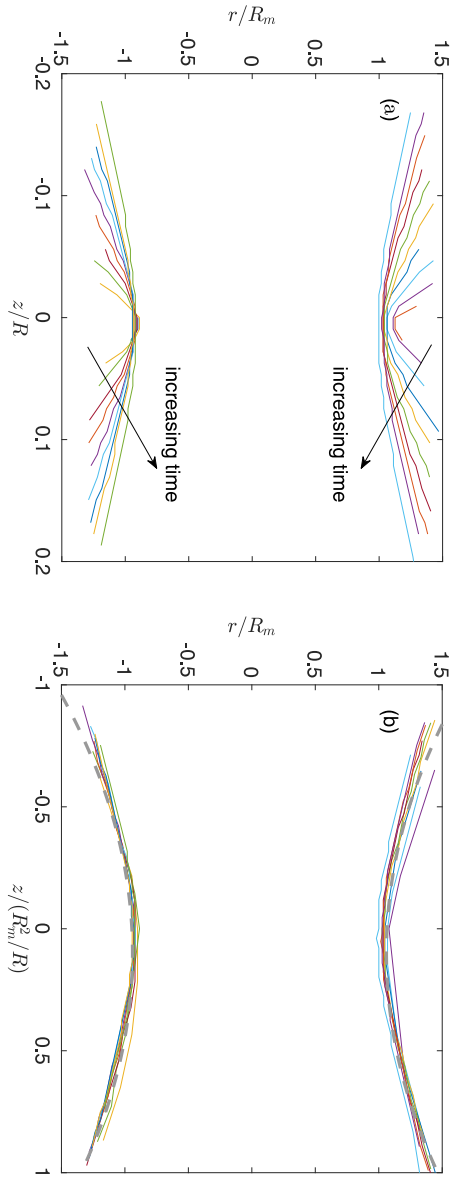

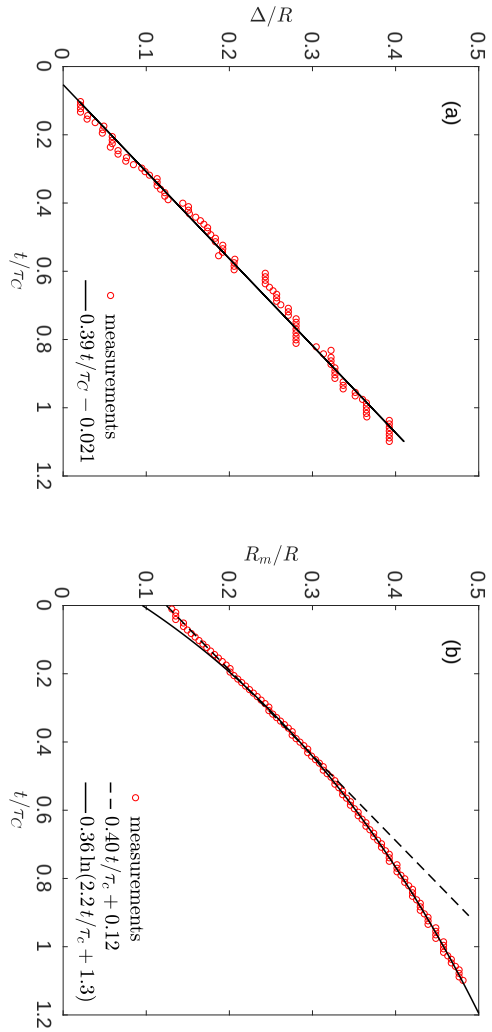

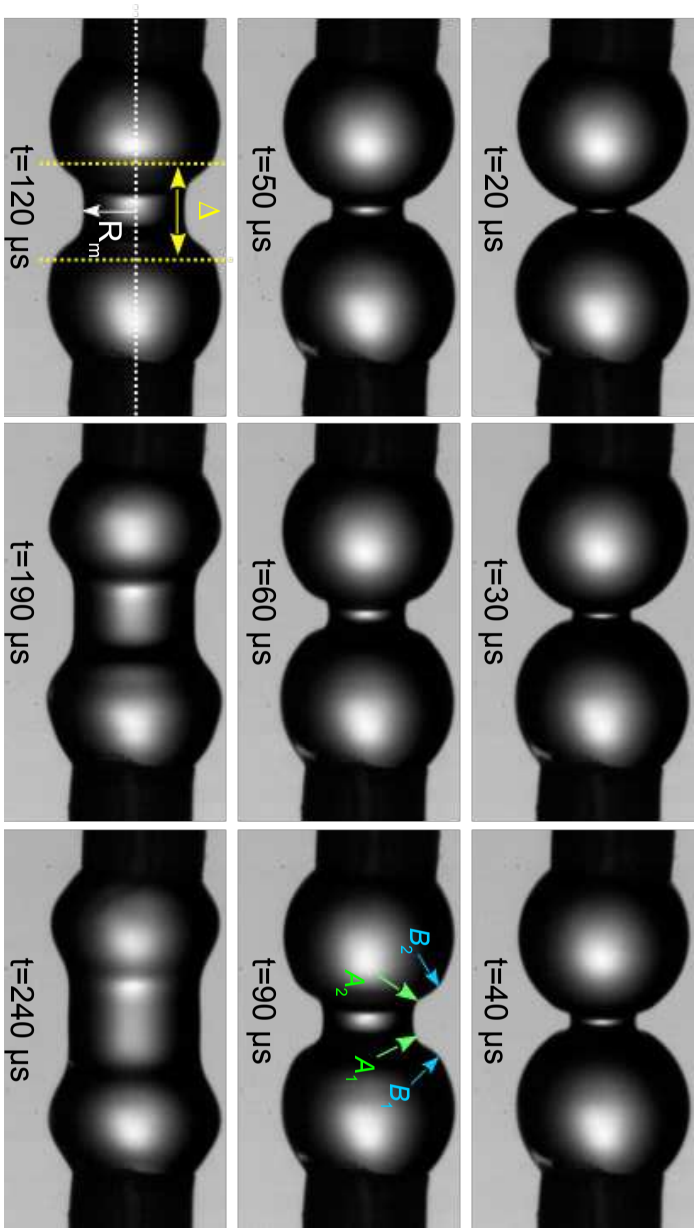

PLEASE CITE THIS ARTICLE AS DOI: 10.1063/5.0055238

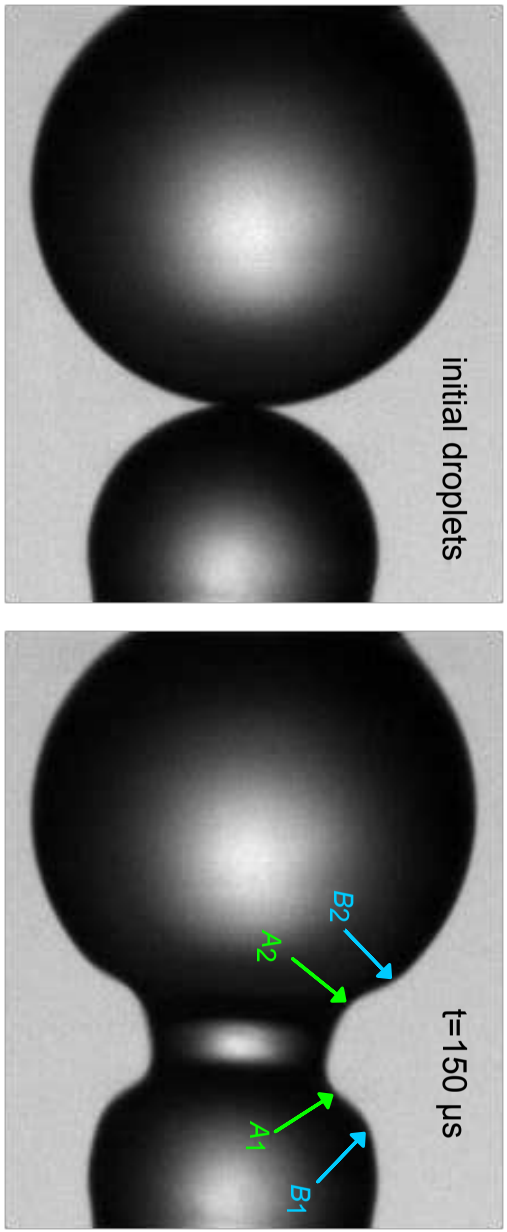

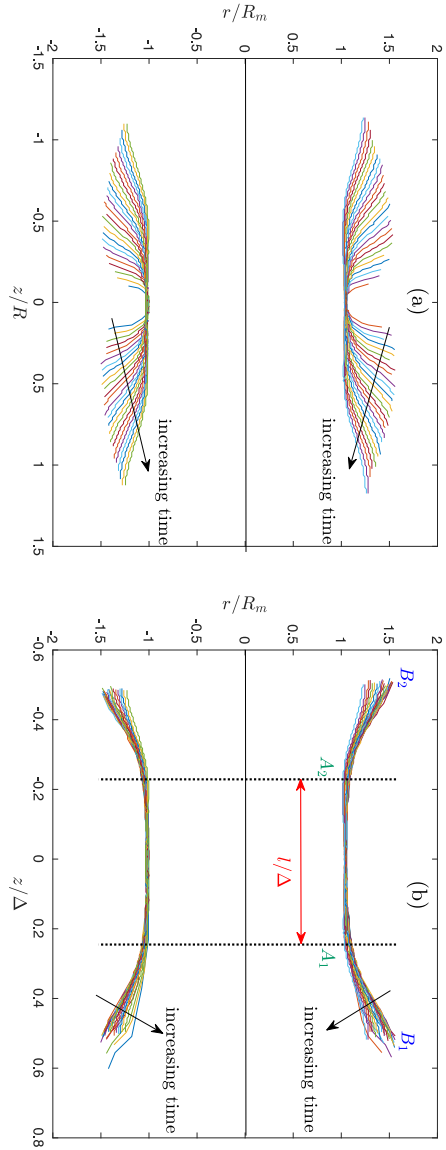

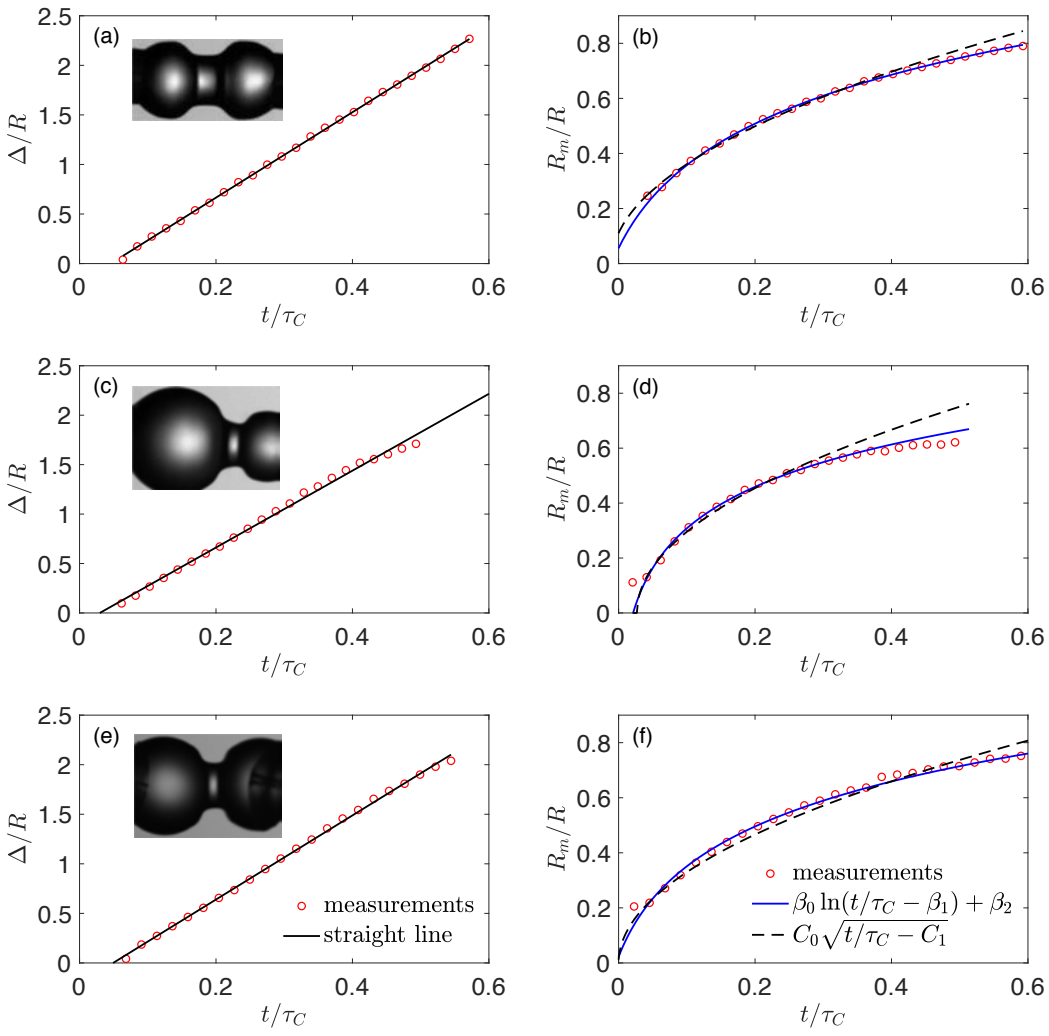

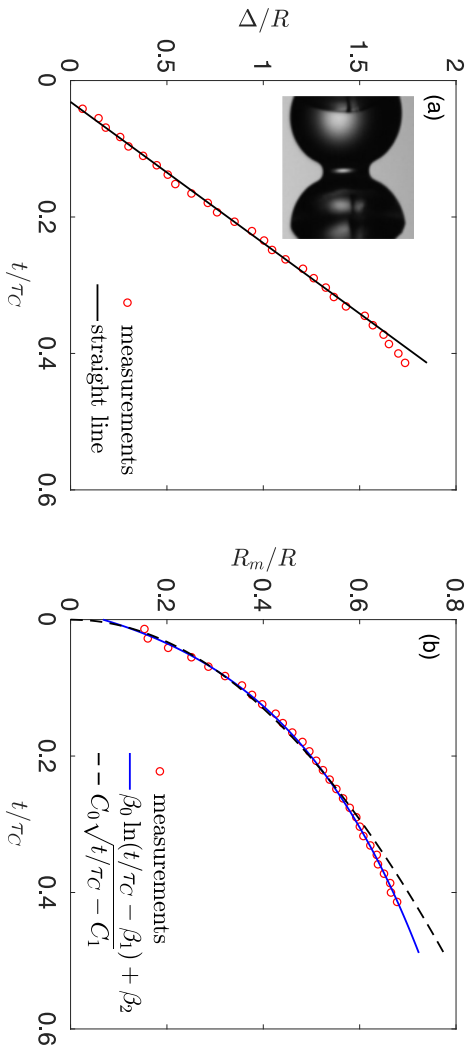

PLEASE CITE THIS ARTICLE AS DOI: 10.1063/5.0055238